



RESEARCH ARTICLE | DECEMBER 02 2024

Speckle-based 3D sub-diffraction imaging of sparse samples through a multimode fiber

Zhouping Lyu ; Shih-Te Hung; Carlas S. Smith ; Lyubov V. Amitonova 



APL Photonics 9, 126104 (2024)
<https://doi.org/10.1063/5.0228988>



Articles You May Be Interested In

Ultrathin visible-light OCT endomicroscopy for *in vivo* ultrahigh-resolution neuroimaging in deep brain

APL Photonics (November 2024)

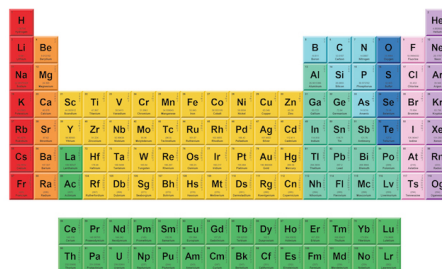
Long-wavelength, high-resolution microscopy using upconversion in ultra-thin crystals

APL Photonics (September 2024)



THE MATERIALS SCIENCE MANUFACTURER®

Now Invent.™



American Elements
 Opens a World of Possibilities

...Now Invent!

www.americanelements.com

© 2021-2024 American Elements & U.S. Registered Trademark

Speckle-based 3D sub-diffraction imaging of sparse samples through a multimode fiber

Cite as: APL Photon. 9, 126104 (2024); doi: 10.1063/5.0228988

Submitted: 16 July 2024 • Accepted: 11 November 2024 •

Published Online: 2 December 2024






View Online



Export Citation



CrossMark

Zhouping Lyu,^{1,2,a)}  Shih-Te Hung,³ Carlas S. Smith,^{3,4}  and Lyubov V. Amitonova^{1,2} 

AFFILIATIONS

¹Advanced Research Center for Nanolithography (ARCNL), Science Park 106, 1098 XG Amsterdam, The Netherlands

²Department of Physics and Astronomy, Vrije Universiteit Amsterdam, De Boelelaan 1081, 1081 HV Amsterdam, The Netherlands

³Delft Center for Systems and Control, Delft University of Technology, Delft, The Netherlands

⁴Department of Imaging Physics, Delft University of Technology, Delft, The Netherlands

^{a)} Author to whom correspondence should be addressed: z.lyu@arcnl.nl

ABSTRACT

A flexible multimode fiber is an exceptionally efficient tool for *in vivo* deep tissue imaging. Recent advances in compressive multimode fiber sensing allow for imaging with sub-diffraction spatial resolution and sub-Nyquist speed. At present, the technology is limited to imaging in a two-dimensional (2D) plane near the fiber distal facet, while in real applications it is very important to visualize three-dimensional (3D) structures. Here, we propose a new approach for fast sub-diffraction 3D imaging of sparse samples through a multimode fiber by using a single 2D scan, speckle illumination, and bucket detection. We experimentally demonstrate precise image plane location as well as 3D imaging of samples with various scattering coefficients. The full width at half maximum of the point spread function along the axial direction is three times smaller than the diffraction limit. Our study grants depth-resolving capacity to ultra-thin super-resolution fiber endoscopes for life science and medical applications.

© 2024 Author(s). All article content, except where otherwise noted, is licensed under a Creative Commons Attribution (CC BY) license (<http://creativecommons.org/licenses/by/4.0/>). <https://doi.org/10.1063/5.0228988>

I. INTRODUCTION

Breakthroughs in biology and life sciences are driven by continuous progress in imaging techniques. Fluorescence imaging has been crucial in this progress, allowing for specific labeling, localization, and visualization of structures of cells and processes with high specificity and sensitivity.^{1,2} Modern super-resolution methods of optical microscopy enable non-destructive imaging with high subcellular spatial resolution.^{3,4} Despite its remarkable capabilities, state-of-the-art super-resolution microscopy has very shallow penetration depth, allowing for imaging of only superficial layers, up to 120 μm deep at best.^{5,6} Moreover, the higher resolution system requires a higher numerical aperture (NA), which makes the point spread function (PSF) more susceptible to scattering. This results in a further reduced penetration depth. In contrast, micro-endoscopes excel at deep imaging as a minimally invasive probe due to their inherently small footprint.^{7,8}

Multimode fibers (MMFs) support the propagation of thousands of spatial modes, providing the highest information density for the given footprint, which is ideal for minimally invasive

endoscopy. However, the information is scrambled by mode mixing and modal dispersion.⁹ Various strategies for two-dimensional (2D) MMF imaging have been proposed utilizing wavefront shaping,^{10,11} speckle imaging,^{12,13} deep learning,^{14,15} and compressive sensing.^{16,17} Random speckle illumination provides a nearly ideal basis for compressive sensing approaches to imaging.¹⁸ Speckle patterns, such as those generated at the MMF output, can be used as structured illumination for super-resolution structural illumination microscopy (SIM).¹⁹ Random speckle illumination can provide a resolution about two times better than that of conventional wide-field microscopy.²⁰ Sparsity-based compressive sensing can further enhance the resolution beyond the physical limit of the microscope for distinct scatterer samples.^{21–23} It has been recently shown that 2D compressive MMF imaging has high-resolution using fewer measurements than the Nyquist limit and is applicable for brain imaging.²⁴

Transitioning from 2D to three-dimensional (3D) imaging is a captivating and impactful progression because the 3D structure of an object contains far more information. 3D imaging through an MMF can be realized by advanced light control: 3D raster scan

at different axial planes,^{25,26} time-of-flight detection,²⁷ and computational reconstruction²⁸ have been demonstrated. However, all these methods rely on wavefront shaping and come with various drawbacks, including complex setup and optimization procedures as well as low imaging speed. Other approaches to reconstructing 3D samples require the knowledge of the full transmission matrix of a fiber to decode depth information based on the propagation of light numerically.^{29,30} These methods either require direct illumination of the sample, limiting the applicability for *in vivo* imaging, or are only effective for coherent imaging, restricting the applicable types of samples to non-fluorescent.

Here, we present 3D imaging of sparse samples through an MMF by using a single 2D raster scan, random-speckle illumination, and single-pixel detection. Three-dimensional information is reconstructed using computational compressive sensing. A three times smaller full width at half maximum (FWHM) of the PSF along the

axial direction than the diffraction limit is shown experimentally. We investigate the robustness of the proposed approach to volumetric light scattering effects and experimentally demonstrate 3D imaging of fluorescence beads in scattering media. The proposed approach is compatible with all kinds of MMF probes, including the flexible multicore-multimode fiber.³¹ Therefore, our work provides an effective, simple, and robust 3D imaging method of sparse samples through an MMF, paving the way for a flexible super-resolution high-speed endoscope.

II. METHODS

A. Experimental setup

The experimental setup is shown in Fig. 1(a). Experiments were performed on a round-core step-index MMF with a diameter of 50 μm and an NA of 0.22 (Thorlabs). The fiber length is around

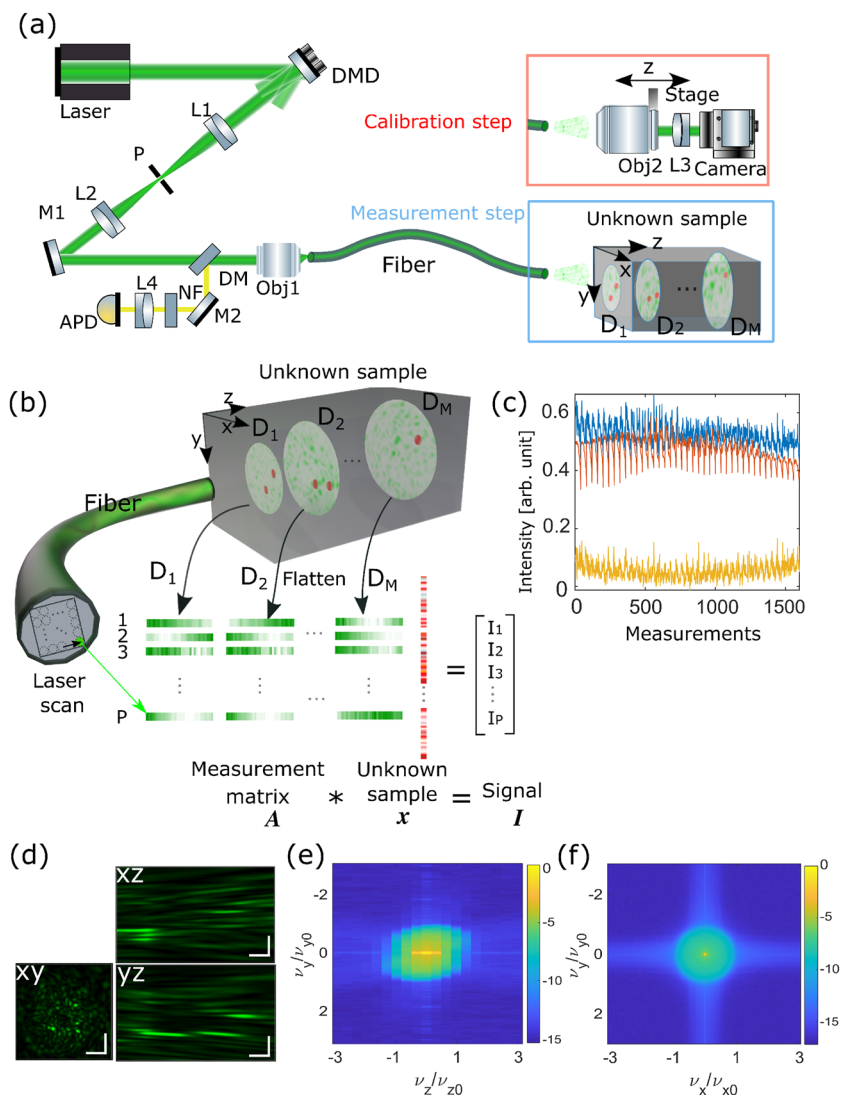


FIG. 1. Illustration of the proposed approach of sub-diffraction 3D imaging through an MMF. (a) Experimental setup. A focused laser beam is scanned across the input facet of the MMF by the DMD. The speckles at various output planes $D_1 \dots D_M$ are captured by the camera during the pre-calibration step, as shown in the red box. The total fluorescence response I_p is collected by the same fiber and registered by the APD. L: lenses, M: mirrors, DMD: digital micromirror device, Obj: objectives, P: pinhole, NF: notch filter, and APD: avalanche photodiode. (b) General idea and computational workflow. For each laser scan position p at the input facet, a 3D speckle pattern illuminates the sample at planes D_1 to D_M . Those P different 3D illumination patterns are flattened, connected head-to-tail, and stacked as a 2D measurement matrix A , consisting of P rows and $M \cdot N^2$ columns. The unknown 3D sample is reshaped to vector x . (c) Signal I (yellow line) is calculated by subtracting the measured intensity without the sample (red line) from the measured intensity with the sample (blue line). (d) The maximum intensity projections in the xy -plane, yz -plane, and xz -plane of a 3D speckle pattern. The scale bars are 10 μm . (e)-(f) Averaged spatial power spectra of the speckle patterns at the MMF output in logarithmic scale. The spectra are shown for the axial, yz plane (e) and lateral, xy plane (f). The frequencies are normalized to the respective theoretical cutoff frequencies.

20 cm. For illumination, we use a continuous wave (CW) linear polarized Nd:YAG laser [Cobolt Samba] with a wavelength of $\lambda = 532$ nm. The laser has a coherence length of 95 m, which is longer than the maximum path length difference in the MMF to form fully developed speckle patterns on the output. The digital micromirror device (DMD) from Texas Instrument, driven by the DLP V-9501 VIS module (Vialux), is used to control the coupling to the MMF. The DMD has a grid of 1920×1080 tilting micromirrors that can rotate individually to $+12^\circ$ (on state) or -12° (off state). By arranging these mirrors in either the on or off state, the DMD can function as a grating, with the grating's orientation determining the laser's position. The DMD pattern is imaged on the back focal plane of objective1 (Olympus, $20\times$, $NA = 0.4$) by a 4f system consisting of lenses L1 ($f_1 = 150$ mm) and L2 ($f_2 = 100$ mm). The pinhole (P1) only allows the +1st diffraction order of the DMD pass. The objective1 couples light to the MMF. Changing the grating direction, the laser beam can be scanned in a zigzag pattern across the fiber input facet. At the distal fiber facet, the speckles at different planes $D_1 \dots D_M$ interact with the sample and excite the fluorescence response. We use a DMD to be able to compare within the same setup the proposed approach with raster-scan imaging experiments based on the wavefront shaping technique, which implements phase or amplitude modulation of the input beam. The DMD has been used solely for the 2D scan of the focused beam at the MMF input facet. One can choose other equipment with a faster response speed, such as an acousto-optical or an electro-optical deflector.

The experimental process is divided into two steps: the calibration step to record the speckles and the measurement step to detect the total excited fluorescence. In the calibration step, objective2 (Leica, $63\times$, $NA = 0.75$) and lens L3 ($f_3 = 250$ mm) image the fiber distal facet on the camera with a total magnification of $79\times$. We use the Basler Ace U acA2040-120 μ m camera with a pixel size of $3.45 \times 3.45 \mu\text{m}^2$, a frame rate of 120 fps, and a resolution of 2048×1536 pixels 2 . To optimize memory usage, the area is cropped to 1200×1200 pixels 2 , and 4×4 pixel 2 binning is applied, resulting in 300×300 pixel 2 images and a recorded speckle plane area of $53 \times 53 \mu\text{m}^2$. By moving the motorized stage (Thorlabs Z912B) with objective2 along the axial direction, different planes $D_1 \dots D_M$ are imaged on the camera. We image speckles for all P scanning positions at the fiber input facet and repeat this process for all M imaging planes by moving objective2. While speckle projection at plane D_1 , located close to the MMF output facet, is recorded in full, speckle projections in other planes are cropped to the central region due to the output beam's expansion with an NA of 0.22. Capturing the full speckle patterns during pre-calibration can further enhance the accuracy of 3D imaging.

In the measurement step, an unknown sample is put right after the MMF. Light from the fiber excites the fluorescence. The total fluorescence response is collected by the same fiber, selected by the dichroic mirror (DM), and focused by lens L4 ($f_4 = 60$ mm) on an avalanche photodiode (Thorlabs APD440A). The notch filter (NF) blocks the pump light. The P intensity values [shown in Fig. 1(c)] are measured twice: once without the sample (red line), and then with the sample (blue line). Subtracting the results of two measurements yields the signal vector (yellow line). The high background comes from various sources, such as fiber autofluorescence and Raman scattering. In this and all following experiments, we kept using the 40×40 2D scanning grid on the fiber input facet and recorded

1600 intensities on the APD. In other words, a 40×40 2D scanning grid generates $P = 40 \times 40 = 1600$ gratings on the DMD, each of them being a 1920×1080 array of binary values that shapes the laser beam wavefront such that it is steered to one of the P positions p at the MMF input facet. The number of measurements, $P = 1600$, is the same for all the experiments. The samples were additionally visualized by a conventional high-NA microscope to provide the reference images.

The expected diffraction-limited axial point spread function defined as FWHM criteria at the fiber output facet can be calculated for our fiber-based microscope as follows:^{32,33}

$$d_z \approx 1.77 \frac{\lambda}{NA_{fiber}^2} \approx 19.5 \mu\text{m}, \quad (1)$$

where NA_{fiber} is the numerical aperture of the MMF. To experimentally characterize the diffraction limit of our imaging system, we have analyzed the spatial frequencies of 3D speckle patterns, $I_n^{speckle}$. The intensity profiles of a 3D speckle pattern in a transverse xy -plane and axial xz -plane and yz -plane are shown in Fig. 1(d). We performed a 2D Fourier transform on the speckle cross section in the xy -plane to determine the lateral resolution and in the yz -plane to address the diffraction limit in the axial (z) direction. The spatial frequency spectrum (S) was computed by taking the squared magnitude of the Fourier transform, $\mathcal{F}\{\cdot\}$. The results were averaged across 100 speckle patterns to obtain a mean power spectrum density,

$$S(v_y, v_{x(z)}) = \left\langle \left| \mathcal{F} \{ I_n^{speckle}(y, x(z)) \} \right|^2 \right\rangle. \quad (2)$$

The spatial frequency distributions of experimentally measured speckle patterns on the MMF output in the axial (yz) and the lateral (xy) directions are presented in Figs. 1(e) and 1(f), respectively. The axes have been normalized to the theoretical diffraction-limited cutoff frequencies, $v_{x0} = v_{y0} = 2NA_{fiber}/\lambda$ and $v_{z0} = NA_{fiber}^2/(1.77\lambda)$. Our results confirm that the cutoff frequencies align with the theoretical diffraction limit. The speckle grain size is measured to be $21.2 \mu\text{m}$ in the axial (z -) direction and $1.2 \mu\text{m}$ in the lateral (xy) direction. More details are [supplementary material](#).

B. Computational reconstruction

The main principle of 3D MMF computational imaging is shown in Fig. 1(b). In contrast to conventional 3D raster scan imaging, the proposed approach does not require point-by-point illumination of the whole 3D region. We computationally reconstruct a 3D image of a sample from the set of total fluorescence intensities collected for a single 2D raster scan performed at the MMF input facet. We use random patterns generated by an MMF and employ the fact that the speckle patterns decorrelate while propagating in free space: the 2D intensity distribution of speckle patterns at different transverse planes on the MMF output is uncorrelated. The analysis of 200 experimentally measured speckle patterns at the MMF output facet presented in S3 of the [supplementary material](#) shows that the cross correlation coefficient drops below 0.3 for two speckle patterns separated along the z -axis by a distance larger than the diffraction limit. A scan on the input fiber facet [marked by the green dot in Fig. 1(b)] gives rise to a complex 3D speckle pattern at the fiber output. Light interaction with the fluorescent sample can

be described as if the fluorophore concentration in each 2D sample plane (D_m) is multiplied by the respective 2D speckle intensity projection. The total fluorescence response, I_p , collected by the same MMF, is the linear combination of the contributions from all 2D planes $D_1 \dots D_M$.

For each scanning point at the input, named as a measurement, the speckles at planes D_1 to D_M are recorded as M matrices with $N \times N$ pixels² and then flattened to M rows of N^2 elements. These vectors are concatenated side-by-side to a single row of $1 \times M \cdot N^2$ elements. The process is repeated P times for P scan points on the input facet, leading to P different 3D illumination patterns and, consequently, P different rows. By combining those P rows vertically, one below the other, one complete measurement matrix A ($P \times M \cdot N^2$) is built as shown in Fig. 1(b). The unknown 3D sample is represented by a one-dimensional vertical vector x ($M \cdot N^2 \times 1$) consisting of M 2D sample planes (from D_1 to D_M), which are flattened and connected one below the other. Finally, the total fluorescence intensities I_p recorded for each scanning position p on the MMF input facet form vector I . As the fluorescent signal is incoherent, the total measured intensity I is a linear sum of the contributions from different points in the sample. As a result, the measurements can be described as a simple linear matrix equation [also illustrated in Fig. 1(b)]

$$Ax = I. \quad (3)$$

Solving this equation gives us x , which is then split and reshaped back to M matrices with $N \times N$ pixels, resulting in a 3D image of the sample. However, since we reconstruct a 3D structure from a single 2D scan, the number of measurements is much smaller than the number of sample pixels: $P \ll M \cdot N^2$. Therefore, the imaging problem converts to solving an underdetermined system of linear equations. When x is *sparse*, meaning that only a few coefficients of the image in a certain basis are nonzero, compressive sensing theory provides unique reconstruction if the measurement matrix A is sufficiently random. If the coefficients of A are independently drawn from a Gaussian distribution, perfect reconstruction can be achieved with only $O(k \log(M \cdot N^2/k))$ measurements, where k is the sparsity level of x . Data processing is regularized through ℓ_1 -norm minimization, which promotes sparsity. Regularization is essential to handle noise and prevent overfitting, ensuring that the recovered signal is both accurate and robust. We use the common SPGL1 solver, which can be accessed and downloaded online.^{34,35} It solves Eq. (3) by

$$\underset{x}{\text{minimize}} \|x\|_1, \quad \text{s.t. } Ax = I, \quad (4)$$

where $\|\cdot\|_1$ is the ℓ_1 -norm. Among the other compressive sensing algorithms, basis pursuit works best when the sample is sparse. We used the central processing unit (CPU) of AMD Ryzen Threadripper 3960X and Matlab 2022b for post-processing and image reconstruction.

C. Sample preparation

We use fluorescently labeled polystyrene beads with a diameter of 1.14 μm to manipulate our 2D and 3D samples. To prepare a 2D sparse sample, the fluorescence beads are first diluted with

de-ionized water. The diluted sample is then placed on a coverslip and left to stand until the water evaporates, completely leaving only the sample.

To prepare a 3D sample that contains both uniform background scatter and distinct scattering objects, we use the following procedure. We first affixed a coverslip with nail polish onto a metal plate with a central hole measuring 18 mm in diameter. Then, we prepared the 0.05% fluorescence stock by diluting the fluorescence bead with de-ionized water, 50% glycerol stock by diluting glycerol with de-ionized water, and 1% agarose stock by diluting agarose powder with de-ionized water. We vortexed the 50% glycerol stock for 1 min to completely mix the glycerol with de-ionized water. Then, we mixed 100 μl 0.05% fluorescence stock, 50 μl 50% glycerol stock, and the corresponding concentration of scatter. The scatter is nanoparticles of zinc oxide with <40 nm average particle size. We added different volumes of scatter to adjust the final concentration of scatter (1:100, 1:250, 1:500, 1:2000, 1:10 000) in the sample. The final concentration of agarose gel is 0.5%. We vortex the mixed stock for 1 min. Then, we add 150 μl 1% agarose stock into the mixed stock and quickly pipette the mixed stock. This step needs to be finished within 10 s to prevent the agarose from becoming solid. Afterward, we added 200 μl of mixed stock to the coverslip, which is affixed to a metal plate. The glycerol in the mixed stock can prevent the agarose from drying out during measurement.

To measure the scattering coefficients of samples with different concentrations, we prepared the same mixed stock as above and added 1 ml of mixed stock to the cuvette. Then, the intensity before the sample and after the sample is measured, as described in S4 of the [supplementary material](#). The scattering coefficients are calculated as [0.18, 0.86, 1.98, 3.52, 7.52] cm^{-1} according to Lambert's law.

III. RESULTS

A. Axial localization of a 2D sample

In the first series of experiments, we demonstrate that the proposed approach allows for imaging a 2D fluorescent sample on the MMF facet and simultaneously precisely locating its axial position. We use a 2D sample prepared as described in Sec. II C, which consists of fluorescent polystyrene particles deposited on a coverslip as presented in Fig. 2(a). As a pre-calibration step, we record matrix A for $M = 2$ planes separated by 30 μm . During the measurements, we record the total fluorescent intensity collected by the MMF for every illumination pattern, I . By solving Eq. (3), we reconstruct two images with 300×300 pixels that correspond to two separate planes along the z -direction. We repeat the same experiment two times, first putting the sample in plane1 (26 μm from the fiber facet) and then in plane2 (56 μm from the fiber facet). The imaging results are presented in Figs. 2(b) and 2(c) for the first and second experiments, respectively. The data are normalized to the maximum detected intensity for both planes for each experiment separately. The 2D sample is visible only at the plane where it was actually placed during the experiment. In Fig. 2(b), the fluorescent beads are reconstructed in the first plane, and the dark background appears in the second plane. The results are opposite if we put the sample in the second plan, as shown in Fig. 2(c). We conclude that the proposed approach can image a 2D sample on the MMF output and simultaneously differentiate the position of its depth.

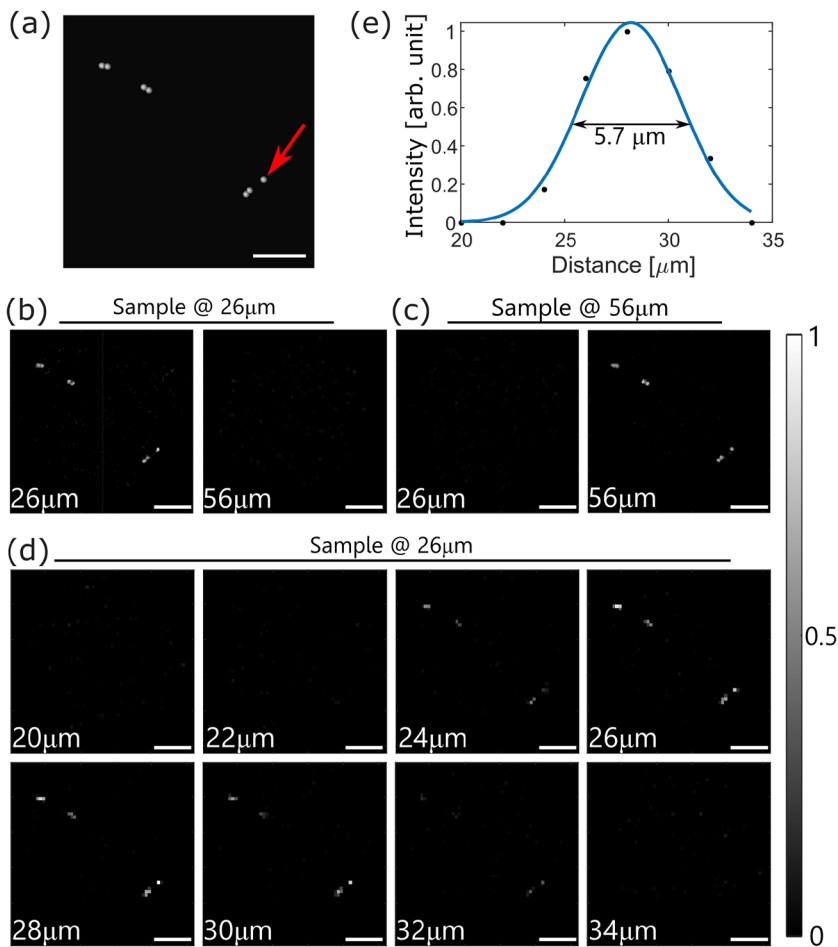


FIG. 2. Experimental results of the proposed MMF imaging and 3D localization approach for a 2D sample. (a) Rendered image of the sample based on high-resolution microscopic image. (b)–(c) Imaging in two planes at a distance of 26 and 56 μm from the MMF facet if the 2D sample is at a 26 μm plane (b) and 56 μm plane (c). (d) The imaging results in eight planes from 20 to 34 μm from the MMF facet. The sample is at 26 μm . The scale bars are 10 μm . (e) Intensity of a single fluorescent bead [marked with the red arrow in (a)] as a function of distance from the MMF output facet: experimental results (black dots) and Gaussian fit (blue line). The FWHM is 5.7 μm .

In the next set of experiments, we use the same 2D sample to characterize the axial resolution of the proposed 3D MMF compressive imaging approach. The 2D sample is put at 26 μm distance from the MMF output facet. The matrix A consists of sub-matrices connected head-to-tail, recorded at eight planes in the z -direction from 20 to 34 μm with a step of 2 μm in between. To decrease the compression rate, the 2D speckles are resized to 59×59 pixels². The images are reconstructed at these planes at once using the single matrix A . The results are shown in Fig. 2(d). The 2D sample is clearly imaged and located at the 26 μm plane where it is supposed to be. We also see that the image is not precise only at 26 μm but blurs forward and backward on the planes from 24 to 32 μm . The more pronounced blurring in the forward direction can be explained by the uncertainty of the sample positioning due to the up to 8 μm backlash of the stage for moving the objective. Correlation analysis of experimentally measured 2D speckle patterns in different planes does not reveal a significant difference between forward and backward directions, as discussed in S3 of the [supplementary material](#). To quantify the effect, we plot the intensity of the brightest fluorescent bead [marked with the red arrow in Fig. 2(a)] as a function of distance in the z -direction. The results are presented in Fig. 2(e) by black circles. A Gaussian fit (shown in blue) reveals a FWHM of 5.7 μm , which is 3 times smaller

than the axial diffraction limit of our MMF-based imaging system according to Eq. (1).

B. 3D imaging experiments

In the next series of experiments, we image a 3D sample that was prepared as described in Sec. II C with zero concentration of background scatters. The sample consists of three fluorescent beads randomly located at different positions in 3D. As a reference, the bright-field images of the sample are recorded with a high-NA microscope objective and LED illumination. The results are presented in the upper row of Fig. 3, where the minimal intensity projections in the xy -plane, yz -plane, and xz -plane are shown. For the proposed fiber-based 3D imaging, we use a single 2D-scan with $P = 1600$ points (single-pixel measurements) on the MMF input and collect the total fluorescent signal. In these experiments, we reconstruct images at $M = 11$ planes with a 2 μm step in-between, starting at 52 μm from the fiber facet. The images are resized to 59×59 pixels². Therefore, the sample is reconstructed within a field of view around $50 \times 50 \times 20$ μm^3 from 1600 single-pixel measurements. The reconstruction results are presented in the lower row of Fig. 3. The

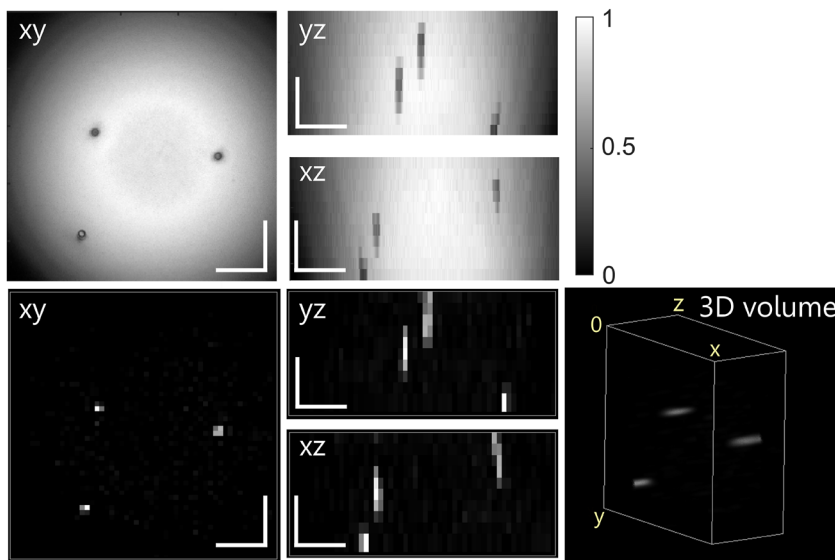


FIG. 3. Experimental results of the proposed 3D imaging through an MMF approach for a 3D sample. The minimum intensity projections of bright field images of the sample in the xy -plane, yz -plane, and xz -plane are presented in the upper row. The maximum intensity projections in the xy -plane, yz -plane, and xz -plane and the 3D volume of the imaging results are shown in the lower row. The scale bars are $10\ \mu\text{m}$.

3D volumetric projection is shown on the right, and the maximum intensity projections in the xy -plane, yz -plane, and xz -plane are shown on the left. The three dots at different depths are reconstructed clearly with an estimated axial width of around $6\ \mu\text{m}$, which matches the previously calculated $5.7\ \mu\text{m}$ from Fig. 2(e).

In the final set of measurements, we experimentally investigate and demonstrate 3D imaging of scattering samples through the MMF by the proposed approach. In biological imaging, one will encounter scattering, bringing two main problems. One is that the speckle illumination of the sample is inconsistent with the measured speckle. Another is that the fluorescence signal is reduced. Therefore, calibrating the behavior of our approach to scattering is important for biological application. As a scatterer, we use zinc oxide nanoparticles added to the 3D sample, as described in Sec. II C. The scattering properties have been characterized in separate experiments as described in S4 of the [supplementary material](#).

The experimental results of 3D imaging of scattering tissues through an MMF are presented in Figs. 4(a)–4(d). Fluorescent beads are embedded into different samples with scattering coefficients of $[0.18, 0.86, 1.98, 3.52]\ \text{cm}^{-1}$. The maximum intensity projections in the xy -plane, yz -plane, and xz -plane are shown in the first, second, and third columns, respectively. The 3D volumes for each sample are presented in the fourth column. The scale bars are $20\ \mu\text{m}$. The axial reconstruction range varies in the scattering samples due to the difficulty of manipulating random 3D samples. As a result, the dimensions of the measurement matrix and the compression rate are different. Bright-field high-NA ground truth images (left) and images recorded through an MMF (right) at various planes in the z -direction are shown in Video 1, 2, and 3 of the [supplementary material](#) for samples with scattering coefficients of $[0.86, 1.98, 3.52]\ \text{cm}^{-1}$, respectively. In bright-field reference images, the presence of a bead is indicated by darker colors. In contrast, in MMF-based imaging, the fluorescent signal from the bead is represented by whiter

colors. In addition, white circles indicate the locations of the beads. Some representative planes where the beads are focused are also shown in S7 of the [supplementary material](#). Comparing the ground truth and the images, we demonstrate the 3D reconstruction within a field of view around $50 \times 50 \times 140\ \mu\text{m}^3$, based on 1600 single-pixel measurements.

C. Numerical simulations

The experimentally measured axial width of the signal of a single bead suggests sub-diffraction resolution. To demonstrate that indeed two points can be differentiated, we performed numerical experiments. In our simulation, three artificial beads with a size of $1, 1, \text{ and } 6\ \mu\text{m}$ along the x -, y -, and z -axis, respectively, are positioned at the same lateral coordinates $(x, y) = (20, 20\ \mu\text{m})$ but at different z -positions of $8, 16, \text{ and } 28\ \mu\text{m}$. Therefore, the separation in the axial direction between neighboring beads was 8 and $12\ \mu\text{m}$. We used an experimentally captured sequence of 40×40 2D speckle patterns across 38 planes, each spaced $2\ \mu\text{m}$ apart. The signal vector was obtained by multiplying the artificially generated 3D sample with the experimentally measured 3D speckle pattern. The results are presented in S2 of the [supplementary material](#). We see that the intensity at the midpoints between the peaks shows a minimum, and therefore all three objects are resolved. Our simulations demonstrate that the proposed imaging method can achieve super-resolution in the axial plane.

We compare the performance of the sparsity-based reconstruction framework with the conventional matrix pseudoinverse for distinct scatterer scenarios. The reconstruction results of the Moore–Penrose inverse algorithm on the same measurement matrix A and signal vector I are shown in S5 of the [supplementary material](#). In contrast to the ℓ_1 -norm minimization algorithm, the pseudoinverse results in a lower signal-to-noise ratio and an almost twice larger FWHM of the axial PSF of $10.3\ \mu\text{m}$.

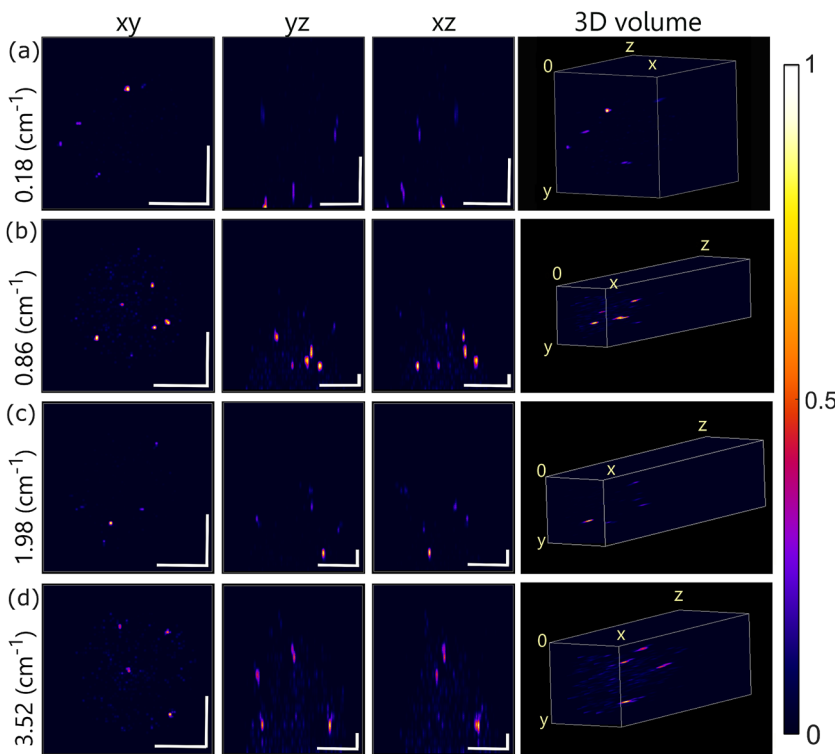


FIG. 4. (a)–(d) Experimental results of the proposed 3D imaging through an MMF approach for 3D scattering samples with scattering coefficients of 0.18 cm^{-1} (a), 0.86 cm^{-1} (b), 1.98 cm^{-1} (c), and 3.52 cm^{-1} (d). The 3D volume projection and the maximum intensity projections in the xy -plane, yz -plane, and xz -plane of the reconstruction are shown. The scale bars are $20 \mu\text{m}$.

We investigate the performance of the proposed approach under noise by adding simulated noise to the measured signal I . The imaging results of basis pursuit and pseudoinverse with signal-to-noise ratios from 25 to 5 dB are shown in S6 of the [supplementary material](#). The ℓ_1 -norm minimization algorithm shows higher noise tolerance by reconstructing the sparse sample with a superior signal-to-background ratio at 5 dB compared to the pseudoinverse at 25 dB.

IV. DISCUSSION AND CONCLUSION

We propose and experimentally demonstrate the new approach of 3D speckle-based compressive imaging through an MMF by a single 2D raster scan and a single-pixel detection. We explore random speckle decorrelation in free space propagation and use a 3D speckle matrix pre-recorded for various depths. The 3D image is reconstructed using computational compressive sensing. A more than a three-fold improvement of the FWHM of the point spread function along the z -direction over the diffraction limit is shown experimentally. The fundamental mechanism for the resolution improvement combines several factors, including the structured illumination microscopy concept employed using random speckle patterns as well as compressive sensing theory that allows sub-diffractive features to be recovered. The main requirement is that the image should be sparse, a specific but very general and wide-spread property of signals that occur almost everywhere in nature.^{18,56}

The speed of the proposed 3D MMF imaging is equal to the speed of a single 2D raster scan. This implies that the imaging

process can be exceptionally fast. Larger 3D volumes require longer time for pre-calibration and post-processing, but this will not impact the measurement time needed for collecting intensity data. It takes about several minutes, limited by the camera frame rate for pre-calibration and CPU for post-processing. However, as pre-calibration is done once before the measurements and post-processing can be done after all the series of measurements, they do not limit the high-speed 3D imaging abilities of the proposed approach. The fast imaging speed is attributed to the use of a compressive sensing algorithm. The scan size determines the number of rows P of the measurement matrix in the compressive sensing algorithm, and the image volume is proportional to $M \cdot N^2$. Therefore, when the scan size is fixed and the imaging volume is increased, it will result in a higher compression rate. A higher compression rate imposes greater demands on sparsity. The required total number of measurements is directly proportional to the sparsity. The experimental imaging speed is limited by the 2D scanning rate of the DMD, the read-out speed, and the sensitivity of the APD. In our experiments, for all 2D samples and 3D samples, the size of the 2D scan was 40×40 and the DMD repetition rate was set to 100 Hz to simplify synchronization and ensure stable data acquisition. It results in a measurement time of about 0.5 min per image. With the maximum DMD speed of 23 kHz and a single 2D scan size of 40×40 , it will take only 70 ms to generate a 3D image, without any changes to the procedure or hardware. This corresponds to video-rate 3D imaging of about 14 volumes per second.

Despite its high potential, the method has limitations. Careful consideration of the compression ratio is necessary, and in 3D imaging, illumination for distant planes may be obstructed by

samples at the same lateral position in nearer planes. The maximum 3D volume is constrained by the fiber size in the lateral plane and the signal collection efficiency in the axial direction for non-scattering samples. For scattering samples, the maximum depth is reduced as the speckles are affected by light scattering within the sample. Currently, the MMF must remain stable between the pre-calibration and measurement steps, as even small perturbations can change the inter-mode interference, leading to changes in speckle patterns at the MMF output. Rigid endo-microscopes hold great application perspectives in neurosciences for deep-brain *in vivo* imaging.¹⁰ Furthermore, several strategies have been proposed recently to mitigate perturbation sensitivity in MMF-based systems for 2D imaging.^{31,37} Our 3D imaging approach is compatible with these 2D solutions, potentially enabling similar robustness to fiber perturbations in 3D imaging scenarios.

The proposed approach technically requires no intricate wave-front shaping, thereby simplifying the overall experimental process and the setup. It is compatible with all kinds of MMFs, including the flexible multicore-multimode fiber probe.³¹ In the pre-calibration step, instead of recording 2D speckle patterns plane-by-plane, 3D intensity distributions at the fiber output can be calculated based on a field at a single plane or intensity patterns at two distinct planes. Our work provides an effective, simple, and robust 3D imaging method through an MMF, paving the way for a flexible 3D super-resolution high-speed endoscope.

SUPPLEMENTARY MATERIAL

See the [supplementary material](#) for the following: (1) Supplement text: More analysis of diffraction limitation, noise analysis, correlation of speckles, and scattering coefficient characterization. (2) Video 1: Video of the comparison between the ground truth and reconstructed results of the scattering sample with a scattering coefficient of 0.86 cm^{-1} . (3) Video 2: Video of the comparison between the ground truth and reconstructed results of the scattering sample with a scattering coefficient of 1.98 cm^{-1} . (4) Video 3: Video of the comparison between the ground truth and reconstructed results of the scattering sample with a scattering coefficient of 3.52 cm^{-1} .

ACKNOWLEDGMENTS

This work has been partially conducted at the Advanced Research Center for Nanolithography, a public-private partnership between the University of Amsterdam, Vrije Universiteit Amsterdam, the Netherlands Organization for Scientific Research (NWO), and the semiconductor equipment manufacturer ASML, and was partly financed by “Toeslag voor Topconsortia voor Kennis en Innovatie (TKI)” from the Dutch Ministry of Economic Affairs. We thank Marco Seynen for his help in programming the data acquisition software.

We acknowledge the Nederlandse Organisatie voor Wetenschappelijk Onderzoek (WISE).

AUTHOR DECLARATIONS

Conflict of Interest

The authors have no conflicts to disclose.

Author Contributions

Zhouping Lyu: Data curation (lead); Formal analysis (lead); Methodology (lead); Software (lead); Validation (lead); Visualization (lead); Writing – original draft (lead); Writing – review & editing (equal). **Shih-Te Hung:** Methodology (equal); Resources (equal); Writing – review & editing (equal). **Carlas S. Smith:** Conceptualization (supporting); Investigation (supporting); Resources (supporting); Writing – review & editing (supporting). **Lyubov V. Amitonova:** Conceptualization (lead); Data curation (supporting); Formal analysis (supporting); Funding acquisition (lead); Investigation (supporting); Methodology (supporting); Project administration (lead); Resources (lead); Software (supporting); Supervision (lead); Validation (equal); Visualization (equal); Writing – original draft (supporting); Writing – review & editing (equal).

DATA AVAILABILITY

The data that support the findings of this study are available from the corresponding author upon reasonable request.

REFERENCES

- V. Ntziachristos, C. Bremer, and R. Weissleder, “Fluorescence imaging with near-infrared light: New technological advances that enable *in vivo* molecular imaging,” *Eur. Radiol.* **13**, 195–208 (2003).
- L. J. Lauwerends, P. B. van Driel, R. J. Baatenburg de Jong, J. A. Hardillo, S. Koljenovic, G. Puppels, L. Mezzanotte, C. W. Löwik, E. L. Rosenthal, A. L. Vahrmeijer, and S. Keereweer, “Real-time fluorescence imaging in intraoperative decision making for cancer surgery,” *Lancet Oncol.* **22**, e186–e195 (2021).
- C. G. Galbraith and J. A. Galbraith, “Super-resolution microscopy at a glance,” *J. Cell Sci.* **124**, 1607–1611 (2011).
- S. W. Hell, S. J. Sahl, M. Bates, X. Zhuang, R. Heintzmann, M. J. Booth, J. Bewersdorf, G. Shtengel, H. Hess, P. Tinnefeld *et al.*, “The 2015 super-resolution microscopy roadmap,” *J. Phys. D: Appl. Phys.* **48**, 443001 (2015).
- N. T. Urban, K. I. Willig, S. W. Hell, and U. V. Nägerl, “STED nanoscopy of actin dynamics in synapses deep inside living brain slices,” *Biophys. J.* **101**, 1277–1284 (2011).
- Y. Jing, C. Zhang, B. Yu, D. Lin, and J. Qu, “Super-resolution microscopy: Shedding new light on *in vivo* imaging,” *Front. Chem.* **9**, 746900 (2021).
- E. R. Andresen, S. Sivankutty, V. Tsvirkun, G. Bouwmans, and H. Rigneault, “Ultrathin endoscopes based on multicore fibers and adaptive optics: A status review and perspectives,” *J. Biomed. Opt.* **21**, 121506 (2016).
- N. Badt and O. Katz, “Real-time holographic lensless micro-endoscopy through flexible fibers via fiber bundle distal holography,” *Nat. Commun.* **13**, 6055 (2022).
- M. Plöschner, T. Tyc, and T. Čížmár, “Seeing through chaos in multimode fibres,” *Nat. Photonics* **9**, 529–535 (2015).
- M. Stibůrek, P. Ondráčková, T. Tučková, S. Turtaev, M. Šiler, T. Pikálek, P. Jákl, A. Gomes, J. Krejčí, P. Kolbábková *et al.*, “110 μm thin endo-microscope for deep-brain *in vivo* observations of neuronal connectivity, activity and blood flow dynamics,” *Nat. Commun.* **14**, 1897 (2023).
- I. T. Leite, S. Turtaev, D. E. Boonzajer Flaes, and T. Čížmár, “Observing distant objects with a multimode fiber-based holographic endoscope,” *APL Photonics* **6**, 036112 (2021).
- Y. Choi, C. Yoon, M. Kim, T. D. Yang, C. Fang-Yen, R. R. Dasari, K. J. Lee, and W. Choi, “Scanner-free and wide-field endoscopic imaging by using a single multimode optical fiber,” *Phys. Rev. Lett.* **109**, 203901 (2012).
- A. M. Caravaca-Aguirre, S. Singh, S. Labouesse, M. V. Baratta, R. Piestun, and E. Bossy, “Hybrid photoacoustic-fluorescence microendoscopy through a multimode fiber using speckle illumination,” *APL Photonics* **4**, 096103 (2019).
- B. Rahmani, I. Oguz, U. Tegin, J.-I. Hsieh, D. Psaltis, and C. Moser, “Learning to image and compute with multimode optical fibers,” *Nanophotonics* **11**, 1071–1082 (2022).

- ¹⁵Y. Chen, B. Song, J. Wu, W. Lin, and W. Huang, “Deep learning for efficiently imaging through the localized speckle field of a multimode fiber,” *Appl. Opt.* **62**, 266–274 (2023).
- ¹⁶L. V. Amitonova and J. F. De Boer, “Compressive imaging through a multimode fiber,” *Opt. Lett.* **43**, 5427–5430 (2018).
- ¹⁷L. V. Amitonova and J. F. de Boer, “Endo-microscopy beyond the Abbe and Nyquist limits,” *Light: Sci. Appl.* **9**, 81 (2020).
- ¹⁸A. Liutkus, D. Martina, S. Popoff, G. Chardon, O. Katz, G. Lerosey, S. Gigan, L. Daudet, and I. Carron, “Imaging with nature: Compressive imaging using a multiply scattering medium,” *Sci. Rep.* **4**, 5552 (2014).
- ¹⁹K. Prakash, D. Baddeley, C. Eggeling, R. Fiolka, R. Heintzmann, S. Manley, A. Radenovic, C. Smith, H. Shroff, and L. Schermelleh, “Resolution in super-resolution microscopy—Definition, trade-offs and perspectives,” *Nat. Rev. Mol. Cell Biol.* **25**, 677 (2024).
- ²⁰E. Mudry, K. Belkebir, J. Girard, J. Savatier, E. Le Moal, C. Nicoletti, M. Allain, and A. Sentenac, “Structured illumination microscopy using unknown speckle patterns,” *Nat. Photonics* **6**, 312–315 (2012).
- ²¹S. Gazit, A. Szameit, Y. C. Eldar, and M. Segev, “Super-resolution and reconstruction of sparse sub-wavelength images,” *Opt. Express* **17**, 23920–23946 (2009).
- ²²P. Sidorenko, O. Kfir, Y. Shechtman, A. Fleischer, Y. C. Eldar, M. Segev, and O. Cohen, “Sparsity-based super-resolved coherent diffraction imaging of one-dimensional objects,” *Nat. Commun.* **6**, 8209 (2015).
- ²³K. Abrashitova and L. V. Amitonova, “High-speed label-free multimode-fiber-based compressive imaging beyond the diffraction limit,” *Opt. Express* **30**, 10456–10469 (2022).
- ²⁴B. Lochocki, M. V. Verweg, J. J. Hoozemans, J. F. de Boer, and L. V. Amitonova, “Epi-fluorescence imaging of the human brain through a multimode fiber,” *APL Photonics* **7**, 071301 (2022).
- ²⁵Z. Wen, Z. Dong, Q. Deng, C. Pang, C. F. Kaminski, X. Xu, H. Yan, L. Wang, S. Liu, J. Tang *et al.*, “Single multimode fibre for in vivo light-field-encoded endoscopic imaging,” *Nat. Photonics* **17**, 679 (2023).
- ²⁶D. Loterie, S. Farahi, I. Papadopoulos, A. Goy, D. Psaltis, and C. Moser, “Digital confocal microscopy through a multimode fiber,” *Opt. Exp.* **23**, 23845–23858 (2015).
- ²⁷D. Stellinga, D. B. Phillips, S. P. Mekhail, A. Selyem, S. Turtaev, T. Čížmár, and M. J. Padgett, “Time-of-flight 3D imaging through multimode optical fibers,” *Science* **374**, 1395–1399 (2021).
- ²⁸Z. Dong, Z. Wen, C. Pang, L. Wang, L. Wu, X. Liu, and Q. Yang, “A modulated sparse random matrix for high-resolution and high-speed 3D compressive imaging through a multimode fiber,” *Sci. Bull.* **67**, 1224–1228 (2022).
- ²⁹S.-Y. Lee, V. J. Parot, B. E. Bouma, and M. Villiger, “Confocal 3D reflectance imaging through multimode fiber without wavefront shaping,” *Optica* **9**, 112–120 (2022).
- ³⁰J. Sun, J. Wu, S. Wu, R. Goswami, S. Girardo, L. Cao, J. Guck, N. Koukourakis, and J. W. Czarske, “Quantitative phase imaging through an ultra-thin lensless fiber endoscope,” *Light: Sci. Appl.* **11**, 204 (2022).
- ³¹Z. Lyu, K. Abrashitova, J. F. De Boer, E. R. Andresen, H. Rigneault, and L. V. Amitonova, “Sub-diffraction computational imaging via a flexible multicore-multimode fiber,” *Opt. Express* **31**, 11249–11260 (2023).
- ³²J. W. Goodman, *Speckle Phenomena in Optics: Theory and Applications* (Roberts and Company Publishers, 2007).
- ³³M. Born and E. Wolf, *Principles of Optics* (Cambridge University Press, 2019).
- ³⁴E. van den Berg and M. P. Friedlander, SPGL1: A solver for large-scale sparse reconstruction, <https://friedlander.io/spgl1> (2019).
- ³⁵E. van den Berg and M. P. Friedlander, “Probing the pareto Frontier for basis pursuit solutions,” *SIAM J. Sci. Comput.* **31**, 890–912 (2009).
- ³⁶M. Elad, *Sparse and Redundant Representations: From Theory to Applications in Signal and Image Processing* (Springer Science & Business Media, 2010).
- ³⁷B. Lochocki, A. Ivanina, A. Bandhoe, J. F. de Boer, and L. V. Amitonova, “Swept-source multimode fiber imaging,” *Sci. Rep.* **13**, 8071 (2023).